



## N-, P-, and S-doped graphene-like carbon catalysts derived from onium salts with enhanced oxygen chemisorption for Zn-air battery cathodes

Xiangjun Zheng<sup>a</sup>, Jiao Wu<sup>a</sup>, Xuecheng Cao<sup>a</sup>, Janel Abbott<sup>b</sup>, Chao Jin<sup>a</sup>, Haibo Wang<sup>a</sup>, Peter Strasser<sup>d</sup>, Ruizhi Yang<sup>a,\*</sup>, Xin Chen<sup>c,\*</sup>, Gang Wu<sup>b,\*</sup>

<sup>a</sup> College of Energy, Soochow Institute for Energy and Materials Innovations, Key Laboratory of Advanced Carbon Materials and Wearable Energy Technologies of Jiangsu Province, Soochow University, Suzhou 215006, China

<sup>b</sup> Department of Chemical and Biological Engineering, University at Buffalo, The State University of New York, Buffalo, New York 14260, United States

<sup>c</sup> The Center of New Energy Materials and Technology, College of Chemistry and Chemical Engineering, Southwest Petroleum University, Chengdu 610500, China

<sup>d</sup> Department of Chemistry, Chemical Engineering Division, Technical University Berlin, Berlin 10623, Germany



### ARTICLE INFO

#### Keywords:

N, P, S-doped graphene  
Onium salts  
Electrocatalysts  
Oxygen reduction  
Zn-air batteries

### ABSTRACT

Compared to currently studied metal-based catalysts, metal-free heteroatom-doped carbon catalysts have many advantages including no issues of degradation and contamination from metal dissolution. Relying on single type of doping usually cannot yield optimal electronic and geometric structures favorable for the oxygen reduction reaction (ORR). Herein, heteroatom N, P, and S simultaneously doped graphene-like carbon (NPS-G) was successfully synthesized from onium salts by a facile one-step pyrolysis method. The resulting metal-free NPS-G catalyst with optimized N, P, and S contents exhibits enhanced catalytic activity towards the ORR in alkaline media, relative to any single doping. In particular, this metal-free catalyst shows an encouraging half-wave potential ( $E_{1/2} = 0.857$  V) comparable to that of metal-based catalysts. It also demonstrates excellent electrochemical stability and methanol tolerance. This catalyst was further studied as a cathode in a primary Zn-air battery, showing exceptional open-circuit voltage (1.372 V) and power density (0.151 W cm<sup>-2</sup>). The NPS-G cathode delivers a specific capacity of 686 mA h g<sub>Zn</sub><sup>-1</sup> at a current density of 10 mA cm<sup>-2</sup> while utilizing 82.2% of the theoretical capacity (835 mA h g<sub>Zn</sub><sup>-1</sup>). The origin of high activity associated with various heteroatom dopings is elucidated through X-ray photoelectron spectroscopy analysis and density functional theory studies. The enhanced chemisorption of oxygen species (\*OOH, \*O and \*OH) onto the dopants of the NPS-G catalysts reduces charge transfer resistance and facilitate the ORR. The porous 2D structure also contributes to the increase of active site density and facile mass transport.

### 1. Introduction

To address the increasing energy crisis and environmental concerns, fuel cells and metal-air batteries have gained considerable attention due to their high energy conversion efficiency and ecological benignity [1–4]. The sluggish oxygen reduction reaction (ORR) kinetics limits the performance of these renewable energy systems. It's well known that Pt-based catalysts, with superior activity, are promising electrocatalysts for the ORR. However, the high cost, scarcity, low selectivity and limited durability of Pt pose a great challenge to the large-scale commercialization of fuel cells and metal-air batteries [5–7].

Precious metal-free electrocatalysts, with high ORR activity and enhanced durability, are crucial for the widespread applications of the fuel cell and metal-air battery technologies. Therefore, it is essential to

develop electrocatalysts derived from earth-abundant elements. In addition, compared to traditional metal-based catalysts, metal-free carbon catalysts are particularly attractive for electrocatalytic ORR due to their low cost, unique physicochemical structure, high electric conductivity, corrosion resistance and environmental acceptability [8,9]. Doping with heteroatoms modulates the electronic surface of carbon and fine tunes the catalytic activity [10]. Both theoretical calculations and experimental studies have confirmed that carbon's ORR activity improves when introducing a heteroatom such as N, P, S, etc. into the carbon lattice. For N-doping, N (3.04)-with higher electronegativity than C (2.55)-breaks the electroneutrality of carbon to create charged sites (C<sup>+</sup>) favorable for O<sub>2</sub> adsorption and enhanced ORR activity. N is a promising *n*-dopant, which can enhance the conductivity of carbon by donating electrons and pushing the Fermi level closer to the conduction

\* Corresponding authors.

E-mail addresses: [yangrz@suda.edu.cn](mailto:yangrz@suda.edu.cn) (R. Yang), [chenxin830107@pku.edu.cn](mailto:chenxin830107@pku.edu.cn) (X. Chen), [gangwu@buffalo.edu](mailto:gangwu@buffalo.edu) (G. Wu).

band. Because of the similar atomic radius of N (70 pm) and C (77 pm), N can easily integrate into the carbon lattice; thus allowing the formation of strong covalent N–C bonds and hence increase the stability of N-doped carbon [11–15]. Compared to N, P has the same number of valence electrons but a higher electron-donating ability due to its larger atomic radius (110 pm). Moreover, the electronegativity of P (2.19) is lower than that of C (2.55), and the charged sites of  $P^+$  are created when P is doped in carbon. In addition, P with a larger atomic radius favors the  $sp^3$ -orbital configuration, generating a high distortion of carbon structures and forming many open edge sites, which enhance the ORR activity of carbon [16–19]. For S-doping, the values of electronegativity for S (2.58) and C (2.55) are very close. Thus, S is unlikely able to significantly break the charge neutrality of carbon. However, the high spin density induced by S-doping in carbon promotes the ORR activity. In addition, the strain-induced charge localization and the lone pairs in the S atoms are also good for oxygen chemisorption [20–23].

Recently, binary [24–26] and ternary [27–29] heteroatom doping suggested a practical approach for improving the ORR activity. Dai and co-workers reported that mesoporous carbon foam co-doped with N and P showed excellent catalytic activity for the ORR in alkaline media, and the first-principle simulation revealed that N and P co-doping was crucial for its high-performance [24]. Wang and co-workers investigated the synergistic effect of S and N co-doping on ORR activity through a variety of characterization techniques and with density functional theory (DFT) calculations [30]. Yu and co-workers synthesized N, P, and S ternary-doped reduced graphene oxide (RGO) by a two-step method; its excellent ORR activity is ascribed to the additional P doping and the synergistic effect on binary N and S-doped RGO by generating active P-N species [27]. Despite the efforts made on metal-free carbon electrocatalysts, the development of reliable and controllable strategies for producing heteroatom-doped carbon with high ORR activity and durability is still a notable challenge [31].

Among various carbon materials, graphene with a laminar structure, high specific surface area, excellent electrical conductivity, and superb chemical stability offers exceptional advantages towards constructing advanced catalysts [32–35]. Doping a heteroatom into graphene is a well-known process that is typically prepared by chemical vapor deposition [36] or modified Hummers' method followed by post-doping heteroatom [37,38]. However, the traditional strategies usually involve tedious and complicated preparation procedures [39]. Thus, facile alternative methods to produce heteroatom-doped graphene with wisely selected precursors are highly desirable. Onium salts are a type of compound that is composed of a cation and an anion with one at least being organic and easy to be functionalized. Because of their charged nature, onium salts usually exhibit a negligible vapor pressure even at high temperatures, showing significant advantages over other carbon precursors [40]. Moreover, incorporated N, S, or P atoms in onium salts usually stay in the carbon network after carbonization [41], which makes onium salts an attractive carbon source with controlled heteroatom dopants.

Herein, onium salts, tetraphenylphosphonium bromide ( $(C_6H_5)_4PBr$ ) and triphenylsulfonium chloride ( $(C_6H_5)_3SCl$ ), are employed for providing carbon, P and S sources, while urea ( $CO(NH_2)_2$ ) acts as the N source and template. A straightforward and controllable synthesis of N, P, and S-doped graphene (NPS-G) via one-pot pyrolysis approach was developed in this work. The resultant NPS-G catalyst with optimized N, P and S content shows an excellent activity and stability in alkaline media for the ORR. X-ray photoelectron microscopy (XPS) and DFT studies further elucidate the origin of the high ORR activity of the NPS-G catalyst. Furthermore, a Zn-air battery has been constructed with the NPS-G catalyst as an air cathode, which demonstrates a high open-circuit voltage and power density comparable to the benchmark of commercial Pt/C (20 wt.%). This work would shed new light on the synthesis of multiple heteroatom doping into carbon from a novel family of onium salts for the applications in energy conversion and storage technologies.

## 2. Experimental section

### 2.1. Catalysts synthesis

The facile synthesis of NPS-G via a simple one-pot approach used onium salts, tetraphenylphosphonium bromide ( $(C_6H_5)_4PBr$ ) and triphenylsulfonium chloride ( $(C_6H_5)_3SCl$ ), as the carbon, P and S sources. Urea ( $CO(NH_2)_2$ ) functioned as the N source and template. Two solutions are created to generate the catalyst product. The first solution contained 2 g of urea dissolved in 10 mL of deionized water and stirred until a transparent solution formed. Then, 0.1 g of  $(C_6H_5)_3SCl$  was added to the first solution. The second solution contained 0.2 g of  $(C_6H_5)_4PBr$  dissolved in 10 mL of ethanol. The two solutions were mixed overnight. The resulting uniform solution was transferred to a refrigerator and dried at  $-47^\circ C$  for 24 h in a lyophilizer. After that, the obtained white powder was sintered in a tube furnace at  $900^\circ C$  with a heating rate of  $3^\circ C \text{ min}^{-1}$  under flowing  $N_2$  and maintained at  $900^\circ C$  for 2 h to completely carbonize the mixture. The final product obtained was a soft black powder of N, P and S ternary-doped graphene, referred to as NPS-G-x for ease of description. The NPS-G-1, NPS-G-2, and NPS-G-3 correspond to samples prepared with the following mass ratios of  $CO(NH_2)_2$  to  $(C_6H_5)_3SCl$  of 40:1, 20:1 and 10:1, respectively. The content of S, therefore the resulting content of N and P, doped in graphene, can be adjusted by changing the mass ratio of  $CO(NH_2)_2$  to  $(C_6H_5)_3SCl$ . Moreover, the best performing sample, NPS-G-2, was further heat-treated at different temperatures. The samples obtained from 700, 800, 900 and  $1000^\circ C$  were noted as NPS-G-2-700, NPS-G-2-800, NPS-G-2-900 and NPS-G-2-1000, respectively. The heating temperature of  $900^\circ C$  is the optimum temperature for carbonization and particularly discussed in the text. For comparison, the N and P co-doped graphene (NP-G) was also synthesized by pyrolyzing the mixture of  $CO(NH_2)_2$  and  $(C_6H_5)_4PBr$  under  $N_2$  atmosphere using the same procedure. The optimized ratio of  $CO(NH_2)_2$  to  $(C_6H_5)_4PBr$  was 10:1. It should be noted that there was nothing left for the pyrolysis of the mixture of  $CO(NH_2)_2$  and  $(C_6H_5)_3SCl$  under  $N_2$  atmosphere using the same procedure. All the as-synthesized samples were washed thoroughly with de-ionized water until no  $Br^-$  or  $Cl^-$  could be detected by a  $AgNO_3$  solution.

### 2.2. Physical characterization

The morphology and microstructure of the synthesized samples were characterized by field emission transmission electron microscopy (TEM) (FEI Tecnai G2 F20 S-TWIN TMP). Atomic force microscopy (AFM) measurements were carried out on a Dimension Icon instrument. The samples used for AFM were prepared by pipetting the dispersion of NPS-G in ethanol onto a clean Si surface and dried at room temperature. Thermogravimetric analysis (TGA) of the samples, performed on PerkinElmer TGA7 in  $N_2$  atmosphere, was calibrated with calcium oxalate. X-ray diffraction (XRD,  $Cu K\alpha$  radiation,  $\lambda = 0.15418 \text{ nm}$ ) measurements were carried out on a Bede D1 X-ray diffractometer with the operating voltage of 40 kV and current of 100 mA. Raman spectroscopy of the samples was performed on a Jobin Yvon LabRAM HR 800 instrument with a 514 nm excitation laser. The nitrogen adsorption/desorption isotherms were measured to obtain the specific surface and the pore size distribution of the samples at liquid nitrogen temperature of  $77^\circ K$  (Quantachrome, QuadraSorb SI). Prior to measurement, the heteroatom-doped graphene samples were dehydrated under vacuum at  $110^\circ C$  overnight. The specific surface area was calculated by the Brunauer-Emmett-Teller (BET) method, and the total pore volume from the amount of  $N_2$  sorption was calculated using the t-plot method. Barrett-Joyner-Halenda (BJH) method was used to calculate the mesopore size distribution and Horvath-Kawazoe (HK) method for the micropores. The binding environment of all the elements in samples was analyzed on an XPS spectrometer (VG ESCALAB MKII) using a monochromatized  $Al K\alpha$  (1486 eV) source. The carbon powder was pressed onto indium (In) metal particles. The spectrum position of each

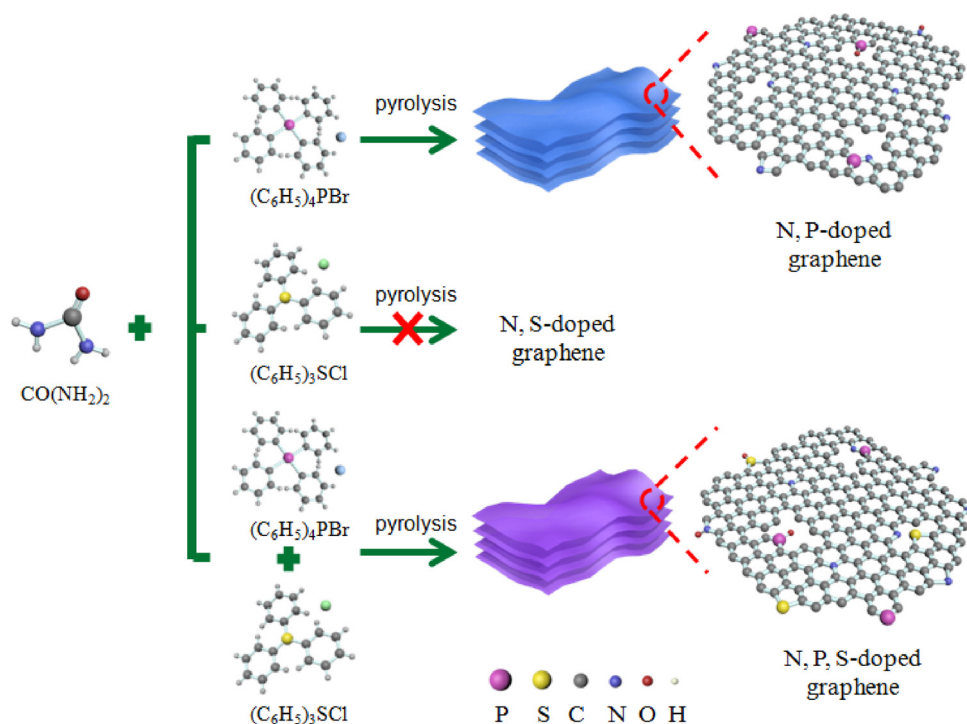


Fig. 1. Schematic illustration of the synthesis of NP-G and NPS-G.

element was calibrated using 284.5 eV as the line position of carbon, which was corrected for the background using the Shirley approach. The surface composition of each sample was determined by measuring the ratio of C 1 s to O 1 s, N 1 s, P 2p and S 2p intensities (integrated peak area) normalized by their respective sensitivity factor [42]. The bulk content of N, P and S in the samples was measured with energy-dispersive X-ray (EDX) analysis.

### 2.3. Electrochemical measurements

The sample's electrocatalytic activity for the ORR was studied with the rotating ring-disk electrode (RRDE) technique using a Pine Electrochemical system (AFMSRX rotator, and AFCBP1 bipotentiostat). The RRDE electrode consisted of glassy carbon (GC) disk ( $0.196\text{ cm}^2$  geometric surface area) surrounded by a Pt ring ( $0.125\text{ cm}^2$  geometric surface area). A standard three-electrode electrochemical cell conducted all the electrochemical tests at room temperature. The catalyst's film-coated GC disk was used as the working electrode, graphite rod as the counter electrode and Hg/HgO as the reference electrode. All of the potential reported in this work have been converted to reversible hydrogen electrode (RHE).. The electrolyte is a 0.1 M KOH solution.. To prepare the catalyst ink for RRDE tests, 5 mg of catalyst powder was dispersed into a solution of 0.350 mL ethanol and 0.095 mL Nafion (5 wt.% from Sigma Aldrich). The ink then underwent ultrasonication for ca. 30 min. Then, 0.007 mL of homogeneous catalyst ink was drop cast onto a 5 mm diameter GC electrode, yielding a catalyst mass loading of  $0.4\text{ mg cm}^{-2}$ . The commercial Pt/C (20 wt.% Pt on graphitized carbon,  $< 5\text{ nm}$  Pt, Sigma Aldrich) electrode was prepared using a similar procedure. The catalyst loading for Pt/C is  $60\text{ }\mu\text{g cm}^{-2}$ . For the ORR test, linear sweep voltammetry (LSV) measurements during oxygen reduction were performed in 0.1 M NaOH electrolyte saturated with high-purity O<sub>2</sub> by sweeping the potential from 0.06 to 0.96 V (vs. RHE) at  $5\text{ mV s}^{-1}$ , where the electrode rotating speed was 400, 900, 1600 and 2500 rpm. For all the RRDE measurements, in order to oxidize HO<sub>2</sub><sup>·</sup> produced during the ORR, the ring potential was held at 1.46 V (vs. RHE) [43]. The electron number (n) and the %HO<sub>2</sub><sup>·</sup> produced transferred during the ORR were calculated using the equations S1 and

S2 (Supporting Information) [44]. The current density was normalized by using the geometric surface area of the disk electrode. The Koutecky–Levich (K–L) plot relates the current density (J) to the angular velocity ( $\omega$ ), which was used to calculate the number of electrons transferred (n) during the ORR process (Eq. S3 and S4 in the Supporting Information) [44,45].

### 2.4. Primary Zn-air battery tests

To prepare the air cathode, 1.0 mg of NPS-G-2 (or 20 wt.% Pt/C) catalyst powder was mixed with 0.25 mg of acetylene black and 10  $\mu\text{L}$  of 5 wt.% Nafion solution, and dispersed in 0.25 mL of ethanol followed by at least 30 min sonication to form a homogeneous ink. This catalyst ink was uniformly dropped cast onto a  $1.0\text{ cm}^2$  hydrophobic carbon paper electrode, to achieve a catalyst loading of  $1.0\text{ mg cm}^{-2}$ , and dried at room temperature. The air cathode was then paired with a polished zinc plate anode and assembled in a customized electrochemical cell filled with 6.0 M KOH containing 0.2 M zinc acetate. Polarization data (V-i) were collected using LSV at a scan rate of  $10\text{ mV s}^{-1}$ . The gas diffusion layer has an effective area of  $1\text{ cm}^2$  and allows O<sub>2</sub> from ambient air to reach the catalyst.

### 2.5. Computational methods

In this work, DFT calculations were carried out using the DMol3 package [46,47]. The well-known generalized-gradient approximation (GGA), with BLYP function, was utilized to describe the exchange and correlation effects [48]. The double numerical plus polarization (DNP) was chosen as the basis set. The effective core potentials (ECP) were used to treat the core electrons of all the atoms. Adsorption energies (E<sub>ads</sub>) are defined as  $E_{\text{ads}} = E_{\text{total}} - E_{\text{catalyst}} - E_X$ , where E<sub>total</sub>, E<sub>catalyst</sub> and E<sub>X</sub> are the total energies of the adsorption system, isolated catalyst, and an adsorbed X species, respectively.

## 3. Results and discussion

As shown in Fig. 1, binary N, P-doped graphene (NP-G) can be

prepared by the pyrolysis of the mixture of  $\text{CO}(\text{NH}_2)_2$  and  $(\text{C}_6\text{H}_5)_4\text{PBr}$ . However, binary N, S-doped graphene (NS-G) can't be synthesized from the mixture of  $\text{CO}(\text{NH}_2)_2$  and  $(\text{C}_6\text{H}_5)_3\text{SCl}$ . To elucidate this phenomenon, TGA was performed. From the data, it can be seen that either  $(\text{C}_6\text{H}_5)_3\text{SCl}$  or the mixture of  $\text{CO}(\text{NH}_2)_2$  and  $(\text{C}_6\text{H}_5)_3\text{SCl}$  is completely decomposed at a temperature greater than 400°C (Fig. S1a and b in the Supporting Information). Interestingly enough, ternary N, P and S-doped graphene (NPS-G) can be obtained from the pyrolysis of  $\text{CO}(\text{NH}_2)_2$ ,  $(\text{C}_6\text{H}_5)_4\text{PBr}$  and  $(\text{C}_6\text{H}_5)_3\text{SCl}$  regardless of the decomposition of  $(\text{C}_6\text{H}_5)_3\text{SCl}$  and  $\text{CO}(\text{NH}_2)_2 + (\text{C}_6\text{H}_5)_3\text{SCl}$  at a high temperature ( $> 400^\circ\text{C}$ ). From the analysis, it's clear that  $(\text{C}_6\text{H}_5)_4\text{PBr}$  plays a key role in the formation of heteroatom-doped graphene. This role can be seen in Fig. S1b in the Supporting Information, although  $\text{CO}(\text{NH}_2)_2 + (\text{C}_6\text{H}_5)_3\text{SCl}$  is completely decomposed, 11.1% of the initial mass is left for  $\text{CO}(\text{NH}_2)_2 + (\text{C}_6\text{H}_5)_4\text{PBr} + (\text{C}_6\text{H}_5)_3\text{SCl}$  even at a high temperature of 800°C. This result indicates that there are remaining amounts of  $(\text{C}_6\text{H}_5)_3\text{SCl}$  after pyrolysis in the presence of  $(\text{C}_6\text{H}_5)_4\text{PBr}$ . The P-doped carbon network, formed from  $(\text{C}_6\text{H}_5)_4\text{PBr}$ , allows other elements formed during pyrolysis to integrate into the structure easily. The intermediates of  $(\text{C}_6\text{H}_5)_3\text{SCl}$  could be incorporated into this carbon network during pyrolysis, resulting in co-doping of S in carbon, while  $\text{CO}(\text{NH}_2)_2$ , as a N source provider, allows the formation of graphene [49].

The morphology and structure of as-prepared samples were investigated via TEM with EDX analysis. All the samples show similar morphology and structure. The typical NPS-G-2 sample exhibits a wrinkled nanosheet structure as manifested by the TEM image (Fig. 2a). As confirmed from the HR-TEM image (Fig. 2b), NPS-G-2 displays an interlayer spacing (ca. 0.35 nm), similar to that of graphene (0.34 nm). The average thickness of the NPS-G-2 is about 2 nm as revealed by the conventional AFM image (Fig. 2c). The STEM image of NPS-G-2 and the corresponding elemental mapping (Fig. 2d) shows the uniform distribution of N, P and S in carbon.

The nitrogen adsorption and desorption measurements were performed to explore the texture properties of NPS-G and NP-G samples. As shown in Fig. 3a, all samples exhibited a combined type I and type IV

isotherm, suggesting that both mesopores and micropores developed in the heteroatom-doped graphene, which can be attributed to the release of H, O and part of N atoms from precursors during the carbonization. NPS-G-2 has a higher BET specific surface area ( $911 \text{ m}^2 \text{ g}^{-1}$ ) than NP-G ( $567 \text{ m}^2 \text{ g}^{-1}$ ), NPS-G-1 ( $775 \text{ m}^2 \text{ g}^{-1}$ ) and NPS-G-3 ( $657 \text{ m}^2 \text{ g}^{-1}$ ), which exposes more active sites. The hierarchical pore structure with mesopores centered at ca. 13.0 nm and micropores centered at ca. 0.78 nm (Fig. 3b and Table S1 in the Supporting Information) in the sample facilitates easy transport of both  $\text{O}_2$  and electrolyte in the triple-phase contact area during ORR.

Fig. S2, in the Supporting Information, shows comparative XRD patterns of the as-synthesized NP-G and NPS-G obtained from different mass ratios of  $\text{CO}(\text{NH}_2)_2$  to  $(\text{C}_6\text{H}_5)_3\text{SCl}$  and heat-treatment temperatures. The XRD patterns all show two broad diffraction peaks for (002) planes at ca.  $25.6^\circ$  and (100) planes at ca.  $43.5^\circ$ . To further evaluate the effect of heteroatom doping on the structure of graphene, Raman analysis was carried out on NPS-G and NP-G. As shown in Fig. 3c, the typical Raman spectra for all the samples can be fitted to four carbon species. Two distinct peaks at about  $1590 \text{ cm}^{-1}$  (G band) and  $1340 \text{ cm}^{-1}$  (D band) are dominant, which correspond to the planar motion of  $\text{sp}^2$ -hybridized carbon atoms in an ideal carbon plane and from carbon atoms at the edge, respectively [50,51]. The peak intensity quantification determined by Raman is also listed in Table S2 in the Supporting Information. The value of  $I_G/I_D$  ratio decreases from NP-G to NPS-G-3, ascribed to more defects caused by more additional S doping. It should be noted that a higher heating temperature during sample synthesis yields a higher value of  $I_G/I_D$ , indicating a higher graphitization degree of carbon (Fig. S3 and Table S2 in the Supporting Information). In addition, two small peaks at around  $1190$  and  $1500 \text{ cm}^{-1}$  are also included in these Raman spectra (Figs. 3c and Fig. S3 in the Supporting Information), which are associated with the carbon atoms outside of a perfectly planar  $\text{sp}^2$  carbon network and heteroatoms in carbon layers or integrated five-number rings, respectively [52]. The peak intensity at around  $1500 \text{ cm}^{-1}$  becomes higher with more doping of S and appears the highest for NPS-G-2, suggesting an increase of

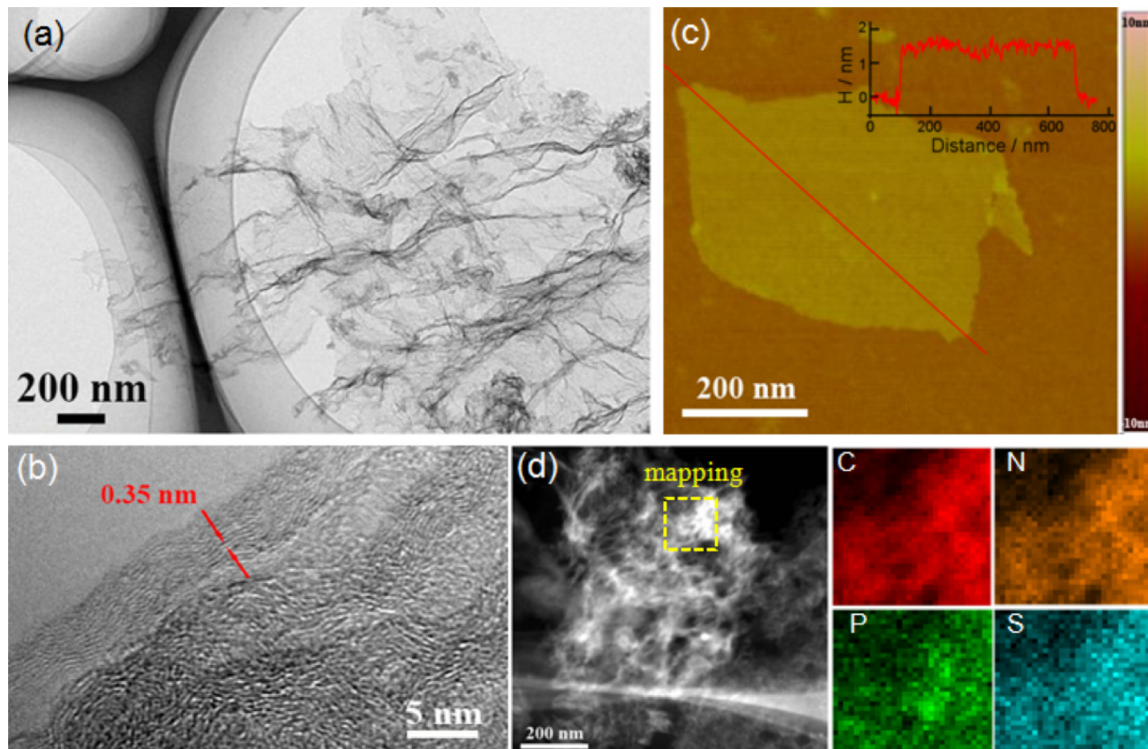
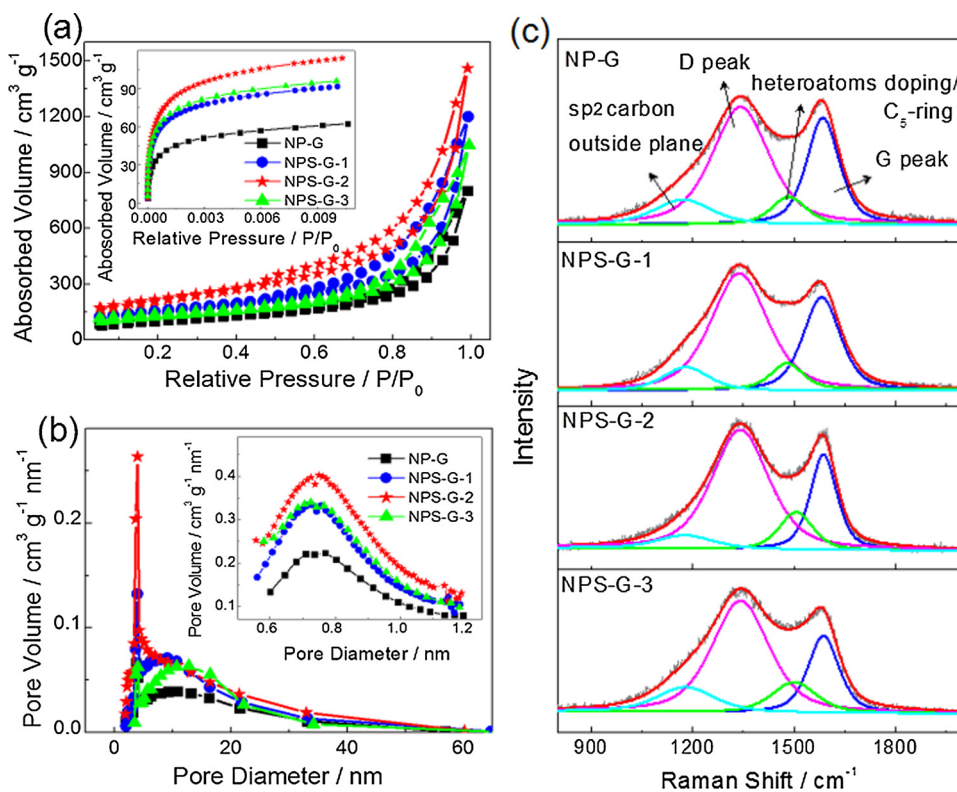


Fig. 2. (a) TEM image of NPS-G. (b) HRTEM image of NPS-G. (c) Typical AFM image of NPS-G. (d) STEM image of NPS-G and the elemental mapping of C, N, P and S in NPS-G.



**Fig. 3.** (a) Nitrogen adsorption and desorption isotherms and (b) corresponding pore-size distributions of samples for mesopore and micropore (insets in a and b). (c) Raman spectra of NP-G, NPS-G-1, NPS-G-2 and NPS-G-3, respectively.

heteroatoms doped and other irregular carbon structures. However, the intensity of the same peak is significantly decreased with an increase in the heating temperature; this is most likely due to more volatilization at high temperatures (Fig. S3 and Table S2 in the Supporting Information). That is, more heteroatoms are evaporated, and the carbon network gets more ordered as the heating temperature increases.

XPS analysis was employed to elucidate the effects of the addition of S doping content and study the binding environment of N, P and S in these carbon catalysts. As expected, the full XPS survey spectrum showed C, O, N, P and S peaks in NPS-G-2 and only C, O, N and P peaks in NP-G (Fig. S4a in the Supporting Information). No Br or Cl signal could be observed from the XPS survey spectra of the samples (Fig. S4a in the Supporting Information), and the effects of Br and Cl atoms on the catalytic activity of the as-synthesized samples are negligible. To probe the bonding configuration and chemical state of N, P and S in the heteroatom-doped graphene, the high-resolution XPS spectra of C 1 s, N 1 s, P 2p, and S 2p were analyzed in detail. As shown in Fig. S4b in the Supporting Information, the fitted peaks for C 1 s of NPS-G series centered at about 284.3, 284.8, 285.6, 286.4, 287.8 and 291 eV are attributed to C–S, C–C, C–P, C–O, C–N and  $\pi$ – $\pi^*$  satellite, respectively [28,53]. These results indicate that N, P and S are successfully doped into the graphene-like carbon. The carbon structures nearly remain the same as more S is doped into carbon. However, when the heating temperature is extended from 700 to 1000°C for NPS-G-2, the relative content of  $\pi$ – $\pi^*$  satellite is significantly increased (Fig. S5a-c and Table S3 in the Supporting Information), which is consistent with the Raman analysis (Fig. S3 and Table S2 in the Supporting Information).

The high-resolution spectra of N 1 s (Fig. 4a) deconvolution into four different peaks, corresponded to pyridinic (398.2 eV), pyrrolic (399.5 eV), graphitic (400.7 eV) and oxidized pyridinic (403.0 eV) nitrogen, respectively [54,55]. A discernable observation of the N-species is that conversion from pyrrolic and pyridinic N to graphitic N occurs upon the additional doping of S into graphene (Fig. 4a and d). Note that the pyridinic-N bonding to two adjacent carbon atoms and graphitic-N

bonding to three can all donate more p electrons to the  $\pi$  system of graphene, which can produce more active sites for oxygen adsorption [56–58]. This observation suggests that S doping helps to create more graphitic N doped in graphene. The content of graphitic and pyridinic N appears the highest for NPS-G-2. Furthermore, the content of graphitic N is visibly increased and gradually dominates at the higher temperature of 900 and 1000 °C (Fig. S6 a and d, and Table S4 in the Supporting Information).

The P 2p spectra shows two typical P species at 133 eV (P-C) and 134 eV (P-O) (Fig. 4b) [39]. The relative content of P-C (active for ORR) is significantly increased from NP-G to NPS-G and reaches the highest for NPS-G-2 (Fig. 4d and Table S5 in the Supporting Information). As shown in Fig. S6b and d in the Supporting Information, the relative content of P-C in NPS-G increases with the increasing of heating temperature and reaches the highest content at 900°C. The deconvolution of S 2p for NPS-G (Fig. 4c) shows three different peaks at the binding energy of 164.0, 165.1 and 168.4 eV, respectively. The former two peaks can be assigned to 2p<sub>3/2</sub> and 2p<sub>1/2</sub> of thiophene-S (active for ORR), while the third peak arises from oxidized S [59]. No other sulfur peak was detected in the S 2p XPS spectrum, suggesting that the S atoms are mainly embedded in the edge and defect sites of graphene in the form of thiophene-S and oxidized S [59,60]. With an increase of S content in the NPS-G samples, the content of oxidized S decreases (Fig. 4d and Table S6 in the Supporting Information), suggesting a better and more successful joining of S atoms into the carbon lattice. Meanwhile, the content of thiophene S (active for ORR) [61] increases and keeps a better combination of S and C at higher temperatures of 900 and 1000 °C (Fig. S6 c and d, and Table S6 in the Supporting Information).

The total contents of N, P and S in the surface layers of these samples from different mass ratios of CO(NH<sub>2</sub>)<sub>2</sub> to (C<sub>6</sub>H<sub>5</sub>)<sub>3</sub>SCl were determined from XPS and are summarized in Fig. 4e. It can be seen that the S content in graphene increases from NPS-1 to NPS-3, that is, it rises with the increasing weight ratio of (C<sub>6</sub>H<sub>5</sub>)<sub>3</sub>SCl to CO(NH<sub>2</sub>)<sub>2</sub>. The P

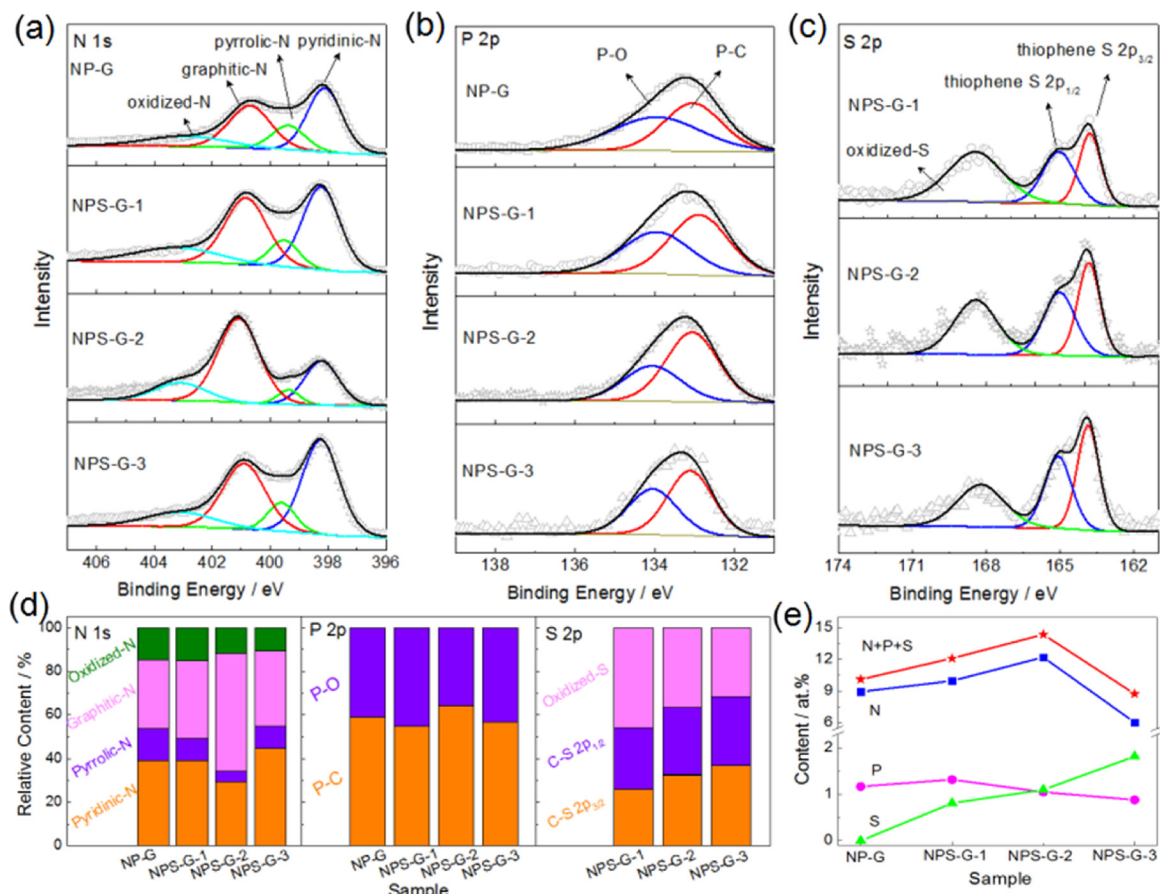


**Fig. 4.** The high-resolution XPS spectra for (a) N 1 s, (b) P 2p and (c) S 2p of NP-G, NPS-G-1, NPS-G-2 and NPS-G-3. (d) The content of different N, P and S species in the NP-G, NPS-G-1, NPS-G-2 and NPS-G-3 derived from the fitted peak of N 1 s, P 2p and S 2p, respectively. Tables have been provided in Supporting Information. (e) The surface content of N, P and S in the samples obtained from XPS.

content grows first then decreases as the S content enlarges. There is a mutual restraint between the P and S content because of their similar radii. The radius of either P or S is larger than that of C, which makes doping of P or S more difficult than doping of N in carbon. With the decreasing content of P, with a low electronegativity, the content of N with higher electronegativity in samples increases first then declines. The results indicate that the N, P and S content in samples can be tuned by controlling the amount of  $(C_6H_5)_3SCl$  in the precursors and mutual restraint between the N, P and S content. The highest content of N, P and S in the NPS-G-2 catalyst has been achieved. Both the dopant species analysis and the total dopant content analysis show the formation of a large number of active sites with high intrinsic activity in NPS-G-2 sample. Furthermore, as shown in Fig. S7 in the Supporting Information, the total surface content of N, P and S decreases from NPS-G-2-700 to NPS-G-2-900, indicating that the heating temperature is important for doping heteroatoms as well as regulating the content of heteroatoms in carbon.

To investigate the electrocatalytic activity of the NP-G and NPS-G samples for ORR, cyclic voltammograms (CV) were first conducted as shown in Fig. S8a in the Supporting Information. NP-G, NPS-G-1, NPS-G-2 and NPS-G-3 samples all show well-defined cathodic oxygen reduction peaks in 0.1 M KOH saturated with  $O_2$ , while they show featureless CVs in the solution saturated with  $N_2$ . The NPS-G-2 exhibits a more positive peak potential of 0.783 V compared to NP-G (0.721 V), NPS-G-1 (0.757 V) and NPS-G-3 (0.742 V). RRDE tests were used to further evaluate the ORR activities of the NP-G and NPS-G samples. For a comparison, the ORR activity of benchmark commercial Pt/C (20 wt. %) was also measured. Fig. 5a shows the LSVs of the samples. The onset potentials are 0.88, 0.93, 0.96 and 0.91 V for the ORR on NP-G, NPS-G-

1, NPS-G-2 and NPS-G-3, respectively. Notably, the half-wave potential of NPS-G-2 (0.857 V) is only 43 mV lower than that of Pt/C (0.900 V). The half-wave potential of the samples follows the order: NPS-G-2 (0.857 V) > NPS-G-1 (0.829 V) > NPS-G-3 (0.808 V) > NP-G (0.774 V). The NPS-G-2 exhibits the best ORR electrocatalytic activity; thus, suggesting an improvement in the activity of N and P co-doped graphene through the additional doping of S.

The electron transfer number ( $n$ ) and corresponding peroxide species ( $HO_2^-$ ) produced on these catalysts during the ORR were calculated according to the RRDE data (Fig. S8b in the Supporting Information) using Eq. S1 and S2 in the Supporting Information, respectively. As can be seen in Fig. 5b, the % $HO_2^-$  yield on the samples follows NPS-G-2 < NPS-G-1 < NPS-G-3 < NP-G over the measured potential range. The electron transfer numbers from the samples show the opposite trend. The two results mentioned previously suggest that the ORR efficiency catalyzed by NPS-G is higher than that by NP-G. The low  $HO_2^-$  yield (below 10%) and high electron transfer number ( $> 3.8$ ) demonstrate a high selectivity of  $4e^-$  ORR on NPS-G-2. Fig. 5c shows the LSVs of the NPS-G-2 at different rotation rates, the polarization plots under four rotation rates all reach well-defined diffusion limited current densities. In the corresponding K-L plots (the inset of Fig. 5c), the approximate parallel to the plot corresponding to  $n = 4$ , the fitted plots at selected potentials suggests that a four-electron pathway is dominant for the ORR on the NPS-G-2 catalyst.

We tested the ORR activity of NPS-G-2 heat-treated at different temperatures of 700, 800, 900 and 1000°C. The NPS-G-2-900 exhibits the highest ORR activity in terms of peak potential shown in CVs, onset potential and half-wave potential shown in LSVs (Fig. S9 in the Supporting Information). When comparing the ORR activity of the best

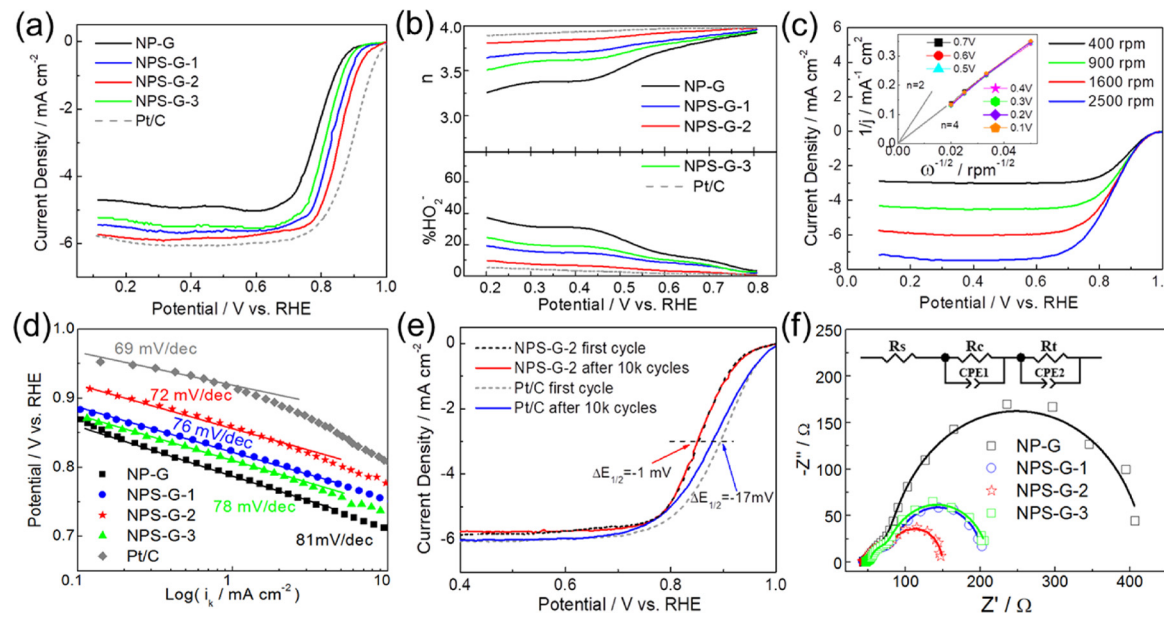


**Fig. 5.** (a) LSVs of NP-G, NPS-G-1, NPS-G-2, NPS-G-3 and commercial Pt/C (20 wt.%) in  $O_2$ -saturated 0.1 M KOH solution at a rotating speed of 1600 rpm. (b) Calculated electron transfer number ( $n$ ) and peroxide yield ( $\%HO_2^-$ ) based on the corresponding RRDE data. (c) Disk current density collected on NPS-G-2 electrode with different rotation speeds during the ORR, inset shows the K-L plots. (d) Tafel plots of NP-G, NPS-G-1, NPS-G-2, NPS-G-3 and commercial Pt/C (20 wt.%) derived by the mass transport correction of corresponding LSV data in (a). (e) LSVs of NPS-G-2 and Pt/C for the first cycle and after 10 000 cycles. (f) Actual and fitting EIS spectra of NP-G, NPS-G-1, NPS-G-2, NPS-G-3, inset shows the equivalent circuit. The catalyst loading for RRDE test is  $60 \mu g cm^{-2}$  and for other tests is  $0.4 mg cm^{-2}$ . The catalyst loading of the Pt/C catalyst is  $60 \mu g cm^{-2}$ .

performing NPS-G-2 catalyst with other reported typical heteroatom-doped graphene catalysts (included in Table S7 in the Supporting Information), the ORR activity of NPS-G-2 is among the best-performing catalysts.

Fig. 5d displays Tafel plots of the ORR for the studied samples. The kinetic currents used for the construction of Tafel plots were derived from the mass-transport correction using the K-L equation (Eq. S3 in the Supporting Information). At low overpotentials, NPS-G-2 shows a Tafel slope of  $72 \text{ mV dec}^{-1}$ , which is smaller than that of NPS-G-1 ( $76 \text{ mV dec}^{-1}$ ), NPS-G-2 ( $78 \text{ mV dec}^{-1}$ ) and NP-G ( $81 \text{ mV dec}^{-1}$ ) and is close to that of Pt/C ( $69 \text{ mV dec}^{-1}$ ). The low Tafel slope indicates the fast kinetics of the ORR on the NPS-G-2 catalyst.

The durability, an important factor for developing a real-world electrocatalyst, was evaluated with potential cycles for the typical sample of NPS-G-2 and commercial Pt/C (Fig. 5e). The cycling was implemented with CV within a potential range of 0.6–1.0 V in  $O_2$ -saturated 0.1 M KOH solution. After 10 000 continuous cycles, the results showed a negligible loss of only 1 mV in the half-wave potential for NPS-G-2, while an observable loss of 17 mV for Pt/C. The durability of NPS-G-2 towards ORR was also assessed by current – time ( $i - t$ ) chronoamperometric measurements and compared with that of commercial Pt/C (20 wt.%). As can be seen in Fig. S10a in the Supporting Information, after 43,200 s (12 h) of continuous operation, Pt/C exhibits a rapid decline in the current by about 47.8%. In contrast, NPS-G-2 retains up to 95.3% of its initial current. NPS-G-2 exhibits much higher stability than Pt/C. The selectivity of ORR against the electro-oxidation of methanol was also measured (Fig. S10b in the Supporting Information). The commercial Pt/C exhibits a sudden change of ORR current due to the electrochemical oxidation of methanol. However, no noticeable change is observed for NPS-G-2 towards ORR, suggesting a high tolerance of NPS-G-2 towards methanol.

EIS was carried out to study the ORR on NPS-G catalysts. The Nyquist plots are shown in Fig. 5f, where the measured impedance spectra data are fitted and analyzed using Zview software. The equivalent circuit is given in the inset of Fig. 5f, where  $R_s$ ,  $R_c$ ,  $R_t$  and CPE represent solution resistance, catalyst film intrinsic resistance,

charge transfer resistance of ORR and constant phase element, respectively. The simulated elemental values are summarized in Table S8 in the Supporting Information. The electrolyte resistance  $R_s$  of the solution (0.1 M KOH) is similar in each measurement, which is all  $9-10 \Omega cm^{-2}$ . The intrinsic resistance  $R_c$  of the NPS-G catalysts decreases with the increase of N + P + S content in graphene, and NPS-G-2 shows the smallest intrinsic resistance ( $4.74 \Omega cm^{-2}$ ). Moreover, the charge transfer resistance  $R_t$  of NPS-G-2 is also the smallest one ( $13.3 \Omega cm^{-2}$ ), while NP-G exhibits the largest charge transfer resistance ( $64.6 \Omega cm^{-2}$ ). Both the smallest intrinsic resistance and charge transfer resistance of NPS-G-2 may result from optimized N, P and S doping in graphene and reasonable electron density redistribution [62,63]. The significantly reduced intrinsic and charge transfer resistance suggest that NPS-G-2 possesses a faster charge-transfer capacity during the ORR.

To further understand why additional doping of S could enhance the ORR catalytic activity of NPS-G, DFT calculations were performed. The optimized structures of NP-G and NPS-G are shown in Fig. S11 in the Supporting Information. The P doping atom, in both structures, is squeezed out of the carbon plane because of its relatively larger radius. Furthermore, due to the larger electronegativity of the doped N atom, positive charges are induced onto its three adjacent C atoms (the Mulliken charge on one of these C atoms is  $+0.206$  for NP-G and  $+0.205$  for NPS-G). On the contrary, the positive charges accumulate onto the P atom ( $+0.562$  for NP-G and  $+0.569$  for NPS-G) and the S atom ( $+0.562$ ) owing to their lower electronegativity. Since the positively charged site is more favorable for adsorbing ORR intermediates, these atoms were simulated as the catalytic sites.

Calculating adsorption energies of ORR intermediates, especially  $^*OOH$ ,  $^*O$ , and  $^*OH$ , is an efficient method to evaluate the ORR activity of catalysts [64–67]. Therefore, we calculated the adsorption energies of  $^*OOH$ ,  $^*O$  and  $^*OH$  on NP-G, NPS-G, and Pt (111) as shown in Fig. 6a, with the values being listed in Table S9 in the Supporting Information. For the sake of clarity, only the structures of adsorbed intermediates on the P site of NPS-G are shown in Fig. 6b. For NP-G, it is observed that the adsorption ability of all ORR intermediates on the N

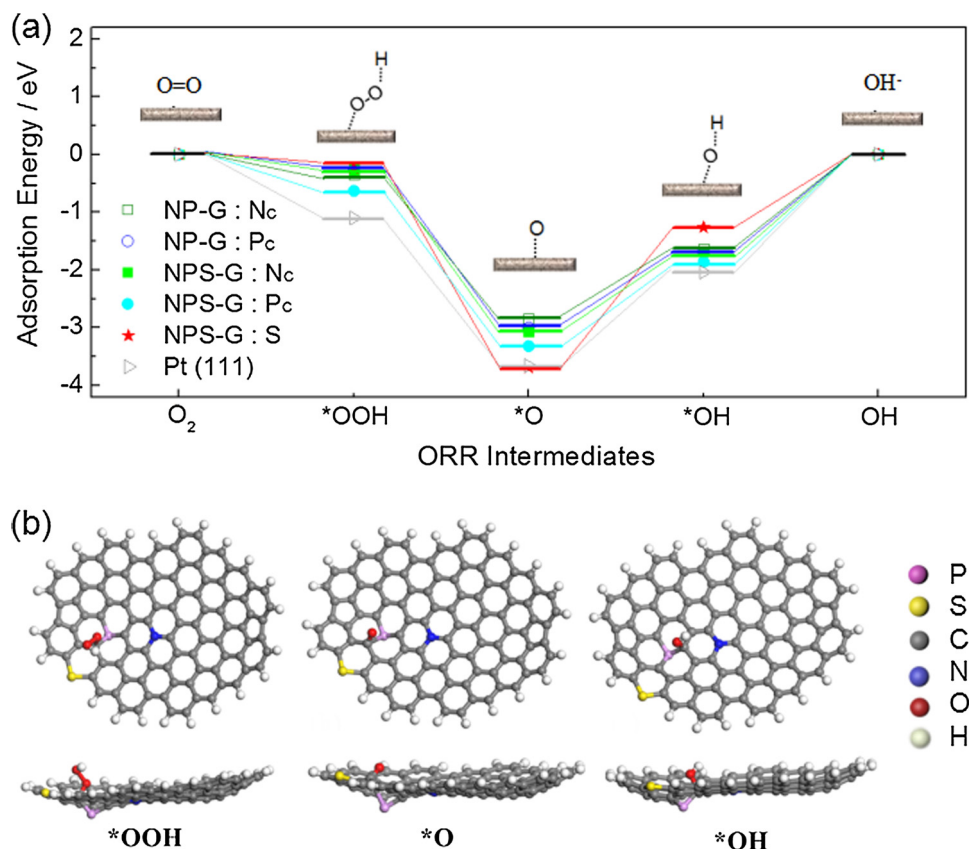


Fig. 6. (a) Calculated adsorption energies of ORR intermediates  $^*OOH$ ,  $^*O$  and  $^*OH$  on NPS-G and (b) the structures of adsorbed  $^*OOH$ ,  $^*O$  and  $^*OH$  on P site of NPS-G.

site is relatively weak when compared with that on Pt (111) (Fig. 6a and Table S9 in the Supporting Information), indicating a limited ORR activity on this site [67]. As for the P site, the  $^*OOH$  group cannot firmly adsorb due to great steric hindrance. The  $^*OOH$  migrates to the C sites adjacent to P dopants. Therefore, the ORR activity of NP-G is low and consistent with the experimental results. But for NPS-G, because of the doping of the S atom, the adsorption ability is significantly enhanced on the P site, which is closer to that of Pt (111). Furthermore, the doped S would also be considered as one of the active sites due to certain adsorption abilities for the ORR intermediates.

Motivated by the outstanding ORR electrochemical performance of the NPS-G-2 catalyst, its effectiveness as an air-cathode for Zn-air batteries was evaluated. A primary Zn-air battery was constructed, in which the NPS-G-2 electrocatalyst-loaded carbon fibre paper was used as the air cathode and paired with a zinc plate in 6.0 M KOH (Fig. 7a). Fig. 7b displays the polarization and power density curves for the Zn-air battery based on the NPS-G-2 air cathode. The NPS-G-2 catalyst shows a peak power density of  $0.151 \text{ W cm}^{-2}$ , comparable to that of commercial Pt/C (20 wt.%) catalyst ( $0.162 \text{ W cm}^{-2}$ ). The open-circuit voltage (OCV) of this primary Zn-air battery is 1.372 V, suggesting a good catalytic performance of NPS-G-2 (inset in Fig. 7c). Notably, the voltage of the battery using NPS-G-2 ( $\sim 1.21 \text{ V}$ ) air cathode at the current density of  $10 \text{ mA cm}^{-2}$  is close to the battery using commercial Pt/C ( $\sim 1.28 \text{ V}$ ) air cathode. Furthermore, no significant voltage drop is observed under galvanostatic discharge at  $10 \text{ mA cm}^{-2}$  for 20 h, owing to the good stability of NPS-G-2 for ORR (Fig. 7c). As shown in Fig. 7d, the specific capacity normalized to the mass of consumed Zn is  $\sim 686 \text{ mAh g}_{\text{Zn}}^{-1}$  at a current density of  $10 \text{ mA cm}^{-2}$ . The value corresponds to an energy density of  $\sim 805 \text{ Wh kg}_{\text{Zn}}^{-1}$  and is  $\sim 82.2\%$  utilization of the theoretical capacity ( $\sim 835 \text{ mAh g}_{\text{Zn}}^{-1}$ ). The galvanostatic discharge voltage plateaus and decreases with increasing current densities (Fig. 7e). At the discharge current densities of 10, 20, 50 and

$100 \text{ mA cm}^{-2}$ , the battery with the NPS-G-2 air cathode shows voltage plateaus of  $\sim 1.21$ ,  $1.17$ ,  $1.06$  and  $0.88 \text{ V}$ , respectively. This is similar to the change of voltage plateaus of Pt/C catalyst. Moreover, as exemplified in Fig. 7f, two series-connected liquid Zn-air batteries based on the NPS-G-2 air cathode are used to power a green LED (2.4 V). It shows excellent operation stability without an obvious change in brightness for 12 h.

The high activity and stability of the NPS-G-2 catalyst can be attributed to the following factors: (i) increased highly active sites induced by N, P and S-doping in graphene, (ii) facilitated chemisorption of oxygen species on NPS-G, (iii) reduced intrinsic and charge transfer resistance, and (iv) high-surface area and porous 2D structure of NPS-G. In principle, ORR activity of a catalyst is directly related to the intrinsic activity of an active site and the site density. Thus, the activity of active sites is enhanced by N-, P- and S-doping in graphene. Meanwhile, the catalytic site density is increased by the high surface area of the NPS-G based carbon. More importantly, the adsorption of oxygen species ( $OOH^*$ ,  $O^*$ , and  $OH^*$ ) plays a decisive role in the surface reactivity of a catalyst. The oxygen reduction kinetics is promoted by the facilitated chemisorption of oxygen species on the NPS-G as evidenced by the DFT calculations. Moreover, the charge transfer during the ORR can be expedited by the reduced intrinsic and charge transfer resistance onto the NPS-G catalyst. The diffusion of  $O_2$  and reactant ions within electrode is facilitated by the porous 2D structure of NPS-G.

#### 4. Conclusions

In summary, the N-, P-, and S- simultaneously doped graphene (NPS-G)-like carbon catalyst has been prepared derived from onium salts through a facile one-step pyrolysis. Both experimental and theoretical results indicate that, due to the favorable chemisorption of oxygen species, reduced intrinsic charge transfer resistance, and porous

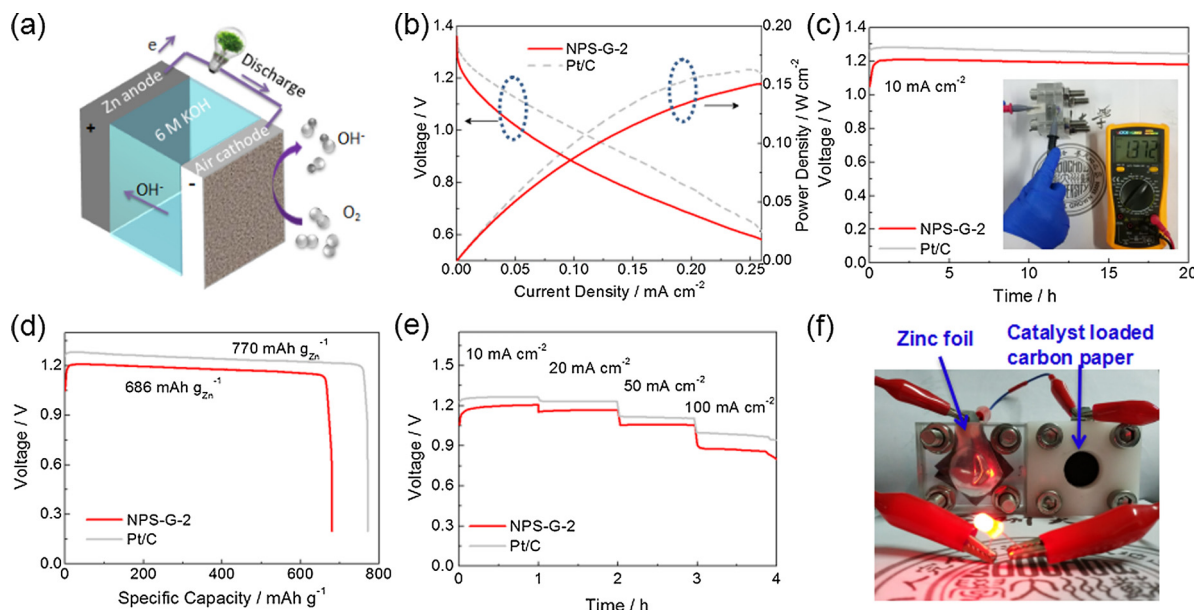


**Fig. 7.** (a) Schematic illustration of the Zn-air battery. (b) Discharge polarization curve and corresponding power density of Zn-air batteries using NPS-G-2 and commercial Pt/C (20 wt.%) as the air-catalyst. (c) Long-term galvanostatic discharge curves of Zn-air batteries using NPS-G-2 and Pt/C as the air-catalyst at 10 mA cm<sup>-2</sup>. Insert photograph of the Zn-air battery with NPS-G-2 as the air catalyst, showing an open-circuit voltage of 1.372 V. (d) Specific capacities of the Zn-air batteries using NPS-G-2 and Pt/C as the air-catalyst that is normalized to the mass of the consumed Zn. (e) Discharge profiles of the Zn-air batteries using NPS-G-2 and Pt/C as the air-catalyst from low current density to high current density (10, 20, 50 and 100 mA cm<sup>-2</sup>). (f) Photograph of a lighted light emitting diode (LED) powered by two liquid Zn-air batteries using the NPS-G-2 as the air cathode connected in series. The catalyst loading is 1 mg cm<sup>-2</sup> on carbon fiber paper.

2D structure, the resultant NPS-G catalyst with optimized N, P and S content exhibits excellent electrocatalytic activity and stability for the ORR in alkaline media. The catalyst shows a high half-wave potential close to that of commercial Pt/C (20 wt.%) catalyst, and presents enhanced electrochemical stability and methanol tolerance. When applying the catalyst as an air cathode for primary Zn-air batteries, it shows high performance comparable to that of benchmark Pt/C. The NPS-G cathode demonstrated a reasonably high open-circuit voltage (1.372 V) and a power density (0.151 W cm<sup>-2</sup>). Moreover, it delivers a specific capacity of 686 mAh g<sub>Zn</sub><sup>-1</sup> at a current density of 10 mA cm<sup>-2</sup>, which is nearly 82% utilization of the theoretical capacity (835 mAh g<sub>Zn</sub><sup>-1</sup>). This work presents a novel approach to prepare advanced metal-free carbon catalysts with multiple heteroatom doping in a control manner, which could be used for electrocatalysis associate with energy storage and conversion technologies.

## Acknowledgements

The authors acknowledge the financial support from the National Key Research and Development Program of China (2016YFB0100200), National Natural Science Foundation of China (Nos. 51572181, 51272167, 21206101 and 51602270), Natural Science Foundation of Jiangsu Province, China (BK20151226). G. Wu also thanks the financial support from National Science Foundation (CBET-1604392).

## Appendix A. Supplementary data

Supplementary material related to this article can be found, in the online version, at doi: <https://doi.org/10.1016/j.apcatb.2018.09.054>.

## References

- [1] G. Wu, K.L. More, C.M. Johnston, P. Zelenay, *Science* 332 (2011) 443–447.
- [2] X.X. Wang, D.A. Cullen, Y.-T. Pan, S. Hwang, M. Wang, Z. Feng, J. Wang, M.H. Engelhard, H. Zhang, Y. He, Y. Shao, D. Su, K.L. More, J.S. Spendelow, G. Wu, *Adv. Mater.* 30 (2018) 1706758.
- [3] Z.Y. Guo, D.D. Zhou, X.L. Dong, Z.J. Qiu, Y.G. Wang, Y.Y. Xia, *Adv. Mater.* 25 (2013) 5668–5672.
- [4] X.X. Wang, S. Hwang, Y.-T. Pan, K. Chen, Y. He, S. Karakalos, H. Zhang, J.S. Spendelow, D. Su, G. Wu, *Nano Lett.* 18 (2018) 4163–4171.
- [5] D. Pan, M. Ombaba, Z.-Y. Zhou, Y. Liu, S.W. Chen, J. Lu, *ACS Nano* 6 (2012) 10720–10726.
- [6] H. Zhang, S. Hwang, M. Wang, Z. Feng, S. Karakalos, L. Luo, Z. Qiao, X. Xie, C. Wang, D. Su, Y. Shao, G. Wu, *J. Am. Chem. Soc.* 139 (2017) 14143–14149.
- [7] G. Wu, A. Santandreu, W. Kellogg, S. Gupta, O. Ogoke, H. Zhang, H.-L. Wang, L. Dai, *Nano Energy* 29 (2016) 83–110.
- [8] K. Gong, F. Du, Z. Xia, M. Durstock, L.M. Dai, *Science* 323 (2009) 760–764.
- [9] D.S. Su, G.Q. Sun, *Angew. Chem. Int. Ed.* 50 (2011) 11570–11572.
- [10] C. Hu, L.M. Dai, *Angew. Chem. Int. Ed.* 55 (2016) 11736–11758.
- [11] H.-W. Liang, X.D. Zhuang, S. Bruller, X.L. Feng, K. Mullen, *Nat. Commun.* 5 (2014) 4973–4979.
- [12] S. Chen, J.Y. Bi, Y. Zhao, L.J. Yang, C. Zhang, Y.W. Ma, Q. Wu, X.Z. Wang, Z. Hu, *Adv. Mater.* 24 (2012) 5593–5597.
- [13] X.J. Zheng, X.C. Cao, X.W. Li, J.H. Tian, C. Jin, R.Z. Yang, *Nanoscale* 9 (2017) 1059–1067.
- [14] D.S. Yu, Q. Zhang, L.M. Dai, *J. Am. Chem. Soc.* 132 (2010) 15127–15129.
- [15] L.M. Dai, Y.H. Xue, L.T. Qu, H.J. Choi, J.B. Baek, *Chem. Rev.* 115 (2015) 4832–4892.
- [16] G. Wu, *Front. Energy* 11 (2017) 286–298.
- [17] C.Z. Zhang, N. Mahmood, H. Yin, F. Liu, Y.L. Hou, *Adv. Mater.* 25 (2013) 4932–4937.
- [18] J. Wu, Z.R. Yang, X.W. Li, Q.J. Sun, C. Jin, P. Strasser, R.Z. Yang, *J. Mater. Chem. A Mater. Energy Sustain.* 1 (2013) 9889–9896.
- [19] Z.W. Liu, F. Peng, H.J. Wang, H. Yu, W.X. Zheng, J. Yang, *Angew. Chem. Int. Ed.* 50 (2011) 3257–3261.
- [20] I.-Y. Jeon, H.-J. Choi, S.-M. Jung, J.-M. Seo, M.-J. Kim, L.M. Dai, J.-B. Baek, *J. Am. Chem. Soc.* 135 (2013) 1386–1393.
- [21] Z.L. Ma, S. Dou, A.L. Shen, L. Tao, L.M. Dai, S.Y. Wang, *Angew. Chem. Int. Ed.* 54 (2015) 1888–1892.
- [22] G.-J. Sohn, H.-J. Choi, I.-Y. Jeon, D.W. Chang, L.M. Dai, J.-B. Baek, *ACS Nano* 6 (2012) 6345–6355.
- [23] Z. Yang, Z. Yao, G.F. Li, G.Y. Fang, H.G. Nie, Z. Liu, X.M. Zhou, X.A. Chen, S.M. Huang, *ACS Nano* 6 (2012) 205–211.
- [24] J.T. Zhang, Z.H. Zhao, Z.H. Xia, L.M. Dai, *Nature Nanotech.* 10 (2015) 444–452.
- [25] Y. Zheng, Y. Jiao, L. Ge, M. Jaroniec, S.Z. Qiao, *Angew. Chem. Int. Ed.* 52 (2013) 3110–3116.
- [26] W. Ai, Z.M. Luo, J. Jiang, J.H. Zhu, Z.Z. Du, Z.X. Fan, L.H. Xie, H. Zhang, W. Huang, T. Yu, *Adv. Mater.* 26 (2014) 6186–6192.
- [27] F. Razmjooei, K.P. Singh, M.Y. Song, J.S. Yu, *Carbon* 78 (2014) 257–267.
- [28] C.H. Choi, S.H. Park, S.I. Woo, *ACS Nano* 6 (2012) 7084–7091.
- [29] X.J. Zheng, X.C. Cao, J. Wu, J.H. Tian, C. Jin, R.Z. Yang, *Carbon* 107 (2016) 907–916.
- [30] X.G. Duan, K.O. Donnell, H.Q. Sun, Y.X. Wang, S.B. Wang, *Small* 11 (2015) 3036–3044.
- [31] J.Y. Cheon, J.H. Kim, J.H. Kim, K.C. Goddeti, J.Y. Park, S.H. Joo, *J. Am. Chem. Soc.* 136 (2014) 8875–8878.

[32] M.A. Worsley, P.J. Pauzauskie, T.Y. Olson, J. Biener, J.H. Satcher, T.F. Baumann, *J. Am. Chem. Soc.* 132 (2010) 14067–14069.

[33] H.-L. Guo, X.-F. Wang, Q.-Y. Qian, F.-B. Wang, X.-H. Xia, *ACS Nano* 3 (2009) 2653–2659.

[34] B.Y. Dai, L. Fu, Z.Y. Zou, M. Wang, H.T. Xu, S. Wang, Z.F. Liu, *Nat. Commun.* 2 (2011) 522–527.

[35] T. Xing, Y. Zheng, L.H. Li, B.C.C. Cowie, D. Gunzelmann, S.Z. Qiao, S.M. Huang, Y. Chen, *ACS Nano* 8 (2014) 6856–6862.

[36] L.T. Qu, Y. Liu, J.-B. Baek, L.M. Dai, *ACS Nano* 4 (2010) 1321–1326.

[37] D.C. Marcano, D.V. Kosynkin, J.M. Berlin, A. Sinitskii, Z.Z. Sun, A. Slesarev, L.B. Alemany, W. Lu, J.M. Tour, *ACS Nano* 4 (2010) 4806–4814.

[38] M. Wei, L. Qiao, H. Zhang, S. Karakalos, K. Ma, Z. Fu, M.T. Swihart, G. Wu, *Electrochim. Acta* 258 (2017) 735–743.

[39] F.P. Pan, J.T. Jin, X.G. Fu, Q. Liu, J.Y. Zhang, *ACS Appl. Mater. Interfaces* 5 (2013) 11108–11114.

[40] K. Daiki, K. Yuiichi, S. Takuma, *J. Photopolym. Sci. Technol.* 29 (2016) 617–622.

[41] S.Y. Liu, Y. Kumatabara, S.J. Shirakawa, *Green Chem.* 18 (2016) 331–341.

[42] D.A. Shirley, *Phys. Rev. B* 5 (1972) 4709–4714.

[43] J. Sunarso, A.A.J. Torriero, W. Zhou, P.C. Howlett, M. Forsyth, *J. Phys. Chem.* 116 (2012) 5827–5834.

[44] U.A. Paulus, T.J. Schmidt, H.A. Gasteiger, R.J. Behm, *J. Electroanal. Chem.* 495 (2001) 134–145.

[45] N.M. MarkovicA, T.J. Schmidt, V. StamenkovicA, P.N. Ross, *Fuel Cells* 1 (2001) 105–116.

[46] B. Delley, *J. Chem. Phys.* 92 (1990) 508–517.

[47] B. Delley, *J. Chem. Phys.* 113 (2000) 7756–7764.

[48] C. Lee, W. Yang, R.G. Parr, *Phys. Rev. B* 37 (1988) 785–789.

[49] J.H. Liu, T.K. Zhang, Z.C. Wang, G.H. Dawson, W. Chen, *J. Mater. Chem.* 21 (2011) 14398–14401.

[50] G. Wu, N.H. Mack, W. Gao, S.G. Ma, R.Q. Zhong, J.T. Han, J.K. Baldwin, P. Zelenay, *ACS Nano* 6 (2012) 9764–9776.

[51] G. Wu, C.M. Johnston, N.H. Mack, K. Artyushkova, M. Ferrandon, M. Nelson, J.S.L. Pacheco, S.D. Conradson, K.L. More, D.J. Myersd, P. Zelenay, *J. Mater. Chem.* 21 (2011) 11392–11405.

[52] S. Mukherjee, D.A. Cullen, S. Karakalos, K. Liu, H. Zhang, S. Zhao, H. Xu, K.L. More, G.F. Wang, G. Wu, *Nano Energy* 48 (2018) 217–226.

[53] Y.Q. Chang, F. Hong, C.X. He, Q.L. Zhang, J.H. Liu, *Adv. Mater.* 25 (2013) 4794–4799.

[54] F.B. Su, C.K. Poh, J.S. Chen, G.W. Xu, D. Wang, Q. Li, J.Y. Lin, X.W. Lou, *Energy Environ. Sci.* 4 (2011) 717–724.

[55] Y. Ito, H.-J. Qiu, T. Fujita, Y. Tanabe, K. Tanigaki, M.W. Chen, *Adv. Mater.* 26 (2014) 4145–4150.

[56] S. Mykola, H.-J. Denisa, Q.L. Gao, T.J. Bandosz, *Carbon* 46 (2008) 1475–1488.

[57] H.J. Kim, K. Lee, S.I. Woo, Y.S. Jung, *Phys. Chem. Chem. Phys.* 13 (2011) 17505–17510.

[58] N. Wang, B.Z. Lu, L.G. Li, W.H. Niu, Z.H. Tang, X.W. Kang, S.W. Chen, *ACS Catal.* 8 (2018) 6827–6836.

[59] S.B. Yang, L.J. Zhi, K. Tang, X.L. Feng, J. Maier, K. Mullen, *Adv. Funct. Mater.* 22 (2012) 3634–3640.

[60] F. Buckel, F. Effenberger, C. Yan, A. Golzhauser, M. Grunze, *Adv. Mater.* 12 (2000) 901–905.

[61] Y.Z. Su, Z.Q. Yao, F. Zhang, H. Wang, Z. Mics, E. Cánovas, M. Bonn, X.D. Zhuang, X.L. Feng, *Adv. Funct. Mater.* 26 (2016) 5893–5902.

[62] J. Liang, Y. Jiao, M. Jaroniec, S.Z. Qiao, *Angew. Chem.* 124 (2012) 11664–11668.

[63] D.W. Wang, D.S. Su, *Energy Environ. Sci.* 7 (2014) 576–591.

[64] F. Sun, X. Chen, *Electrochim. Commun.* 82 (2017) 89–92.

[65] X. Chen, J. Chang, Q. Ke, *Carbon* 126 (2018) 53–57.

[66] X. Chen, *Phys. Chem. Chem. Phys.* 17 (2015) 29340–29343.

[67] X. Chen, F. Sun, J. Chang, *J. Electrochem. Soc.* 164 (2017) 616–619.